# Eliminating Dissolution of Pt-based Electrocatalysts at the Atomic Scale

Pietro P. Lopes[1], Dongguo Li[1], Haifeng Lv[1], Chao Wang[2], Dusan Tripkovic[1,3], Yisi Zhu[1], Roberto Schimmenti[4], Hideo Daimon[5], Yijin Kang[1], Joshua Snyder[6], Nigel Becknell[1], Karren L. More[7], Dusan Strmcnik[1], Nenad M. Markovic[1], Manos Mavrikakis[4] and Vojislav R. Stamenkovic[1,*]

[1] Materials Science Division, Argonne National Laboratory, Lemont, IL 60439, United States
[2] Department of Chemical Engineering, John Hopkins University, Baltimore, MD 21218, United States
[3] Faculty for Technology and Metallurgy, University of Belgrade, Belgrade 11000, Serbia
[4] Department of Chemical and Biological Engineering, University of Wisconsin-Madison, Madison, WI 53706, United States
[5] Faculty of Science and Engineering, Doshisha University, Kyoto, 610-0321, Japan
[6] Department of Chemical Engineering, Drexel University, Philadelphia, PA 19104, United States
[7] Center for Nanophase Materials Sciences, Oak Ridge National Laboratory, Oak Ridge, TN 37831, United States

*Correspondence to: vrstamenkovic@anl.gov

## Abstract

**A remaining challenge for deployment of proton-exchange membrane fuel cells is the limited durability of Pt-nanoscale materials that operate at high voltages during the cathodic oxygen reduction reaction. In this work, atomic-scale insight into well-defined single crystalline, thin-film, and nanoscale surfaces exposed Pt dissolution trends that governed the design and synthesis of durable materials. A newly defined metric, *intrinsic dissolution*, is essential to understanding the correlation between the measured Pt loss, surface structure, size and ratio of Pt-nanoparticles in carbon support. It was found that utilization of Au underlayer promotes ordering of Pt surface atoms towards (111)-structure, while Au on the surface selectively protects low-coordinated Pt sites. This mitigation strategy was applied towards 3 nm $Pt_3Au$/C nanoparticles, resulting in elimination of Pt dissolution in liquid electrolyte, including 30-fold durability improvement vs. 3 nm Pt/C over extended potential range up to 1.2 V.**

The high efficiency of polymer electrolyte membrane fuel cells (PEMFC) to convert the chemical energy stored in hydrogen fuel into electrical power makes them an attractive power source for a variety of transportation systems[1–3]. While the development of PEMFCs over the past 30 years has now led to the commercialization of fuel cell vehicles[4], the road to mass-market remains largely unpaved. In addition to an underdeveloped hydrogen infrastructure, current state-of-the-art Pt-based electrocatalysts still require substantial improvement in performance to decrease stack cost and increase device lifetime. The main limitations reside with the cathode due to both the kinetic barriers of the oxygen reduction reaction (ORR) and durability of employed materials [5]. Strategies to improve kinetics have been derived from atomic level insights towards nano-engineered Pt-based alloys [6–15] with distinct Pt-skin surfaces, which to date are the most active ORR catalysts [16]. Nevertheless, the atomic level approach has offered just mere observations of degradation processes [17–22], but has not provided sufficient guidance in materials design to effectively address durability.

The current picture of catalyst degradation comes from observing metal dissolution, particle size changes, and carbon support corrosion during or after an accelerated stress test (AST) [17,18,27,19–26]. The AST typically induces a decrease in electrochemically active surface area (ECSA) that is particularly exaggerated for small particles (e.g. 3 nm and below) [28–32]. These changes are often rationalized thermodynamically by Ostwald ripening and Gibbs-Thompson effects, but provide little-to-no insight into the key physicochemical parameters and the processes that govern degradation. Only recently with the advent of *in situ* monitoring of Pt dissolution [24,33–35] it was possible to identify and quantify the mechanisms of Pt dissolution at the atomic scale. Electrochemical measurements in combination with mass spectrometry and atomic-scale imaging enabled following Pt dissolution directly from single crystalline surfaces under conditions relevant to ORR [34]. A strong dependence between the geometry of the topmost surface atoms and dissolution has been found, directly correlating to their average coordination number. The (110) structure with low-coordinated surface atoms is the most prone to dissolution, while the most stable (111) surface has the highest coordination of atoms. However, insight into the atomic scale dissolution mechanism on real-world Pt nanoscale catalysts where dissolution/redeposition [36–38] is operative remains elusive. Thus, the establishment of such a functional link is needed to aid the development of viable mitigation strategies.

Here, the dissolution processes on extended single crystalline and thin film surfaces of Pt are correlated to nanomaterials that have well-defined particle size and Pt:C ratio to benchmark intrinsic dissolution rates. The governing Pt dissolution mechanism was mitigated at the atomic scale by addition of less oxophilic Au. The promotion of Pt stability is linked to Au atom placement, both as a subsurface and surface spectator. Ultimately, this led to the design and synthesis of a PtAu nanoscale catalyst with tailored compositional gradients and absence of dissolution at ORR relevant conditions.

Selected Pt electrocatalysts were synthesized through solvothermal synthesis as monodisperse nanoparticles (NPs) with controlled particle size of 3, 5 and 7 nm (Figures 1a, b, c and S1), which enabled to vary the average coordination number of nanoparticle surface atoms [33,34]. Additional obstacle to address is the morphology of the fuel cell electrode layer , which is consisted of catalyst particles, carbon support and tens of nanometer thick ionomer distributed throughout electrode layer for optimal reactant, water, and proton transport [39,40]. However, this porous morphology might affect the assessment of Pt dissolution by confined evolution of dissolved Pt ions and promotion of redeposition during potential cycling. In order to investigate this effect, monodisperse particles of the same catalysts are loaded onto high surface area carbon supports with targeted Pt:C ratio of 20 and 50 wt.%. Measurements of dissolution rates were done *in situ* during cyclic voltammetry experiments in 0.1 mol $L^{-1}$ $HClO_4$ at 50 mV $s^{-1}$ by conjoined stationary probe rotating disk electrode and inductively coupled plasma mass spectrometer (SPRDE-ICP-MS) with detection limits for Pt of 1 ppt (parts per trillion), corresponding to $1x10^{-6}$ ML (atomic monolayer) or 0.4 $pg_{Pt/Au}$ $cm^{-2}$ $s^{-1}$ [34]. The CV protocol was set to allow monitoring of Pt dissolution unimpeded by enhanced redeposition rates induced during fast potential transients [36,37].

The RDE cyclic voltammetry (CV) profiles for the selected Pt/C catalysts deposited in the form of thin layer with equal amount of Pt mass over glassy carbon electrode (see methods), shown in Figures 1d, e and f, represent the typical Pt-adsorbate interactions in aqueous electrolytes ($H_{upd}$ and $OH_{ad}/O_{ad}$) [41]. Equal Pt loading is confirmed by variation of the ECSA from one particle size to another, as reflected by the different $H_{upd}$ charges between 3 to 5 nm, and similar $H_{upd}$ charge for different Pt:C ratios but same particle size, e.g. 5 nm (Figure 1g). As the upper potential limit (1.0 V) is sufficient to cause $PtO_{ad}$ formation, it can also trigger Pt

dissolution events that are characterized by limited anodic dissolution (positive sweep), and significant Pt ion release during the sweep towards lower potentials following PtO reduction near 0.8 V. While the overall dissolution curve profiles are similar, there is an obvious trend in the amount of dissolved Pt, which is retrieved by integration of the dissolution curves in Figures 1d, e and f ($\Gamma_{Pt}$), as summarized in Figure 1h. Higher dissolution is observed for smaller particles (ca. 44.8 pg $cm^{-2}$ for 3 nm versus 3.9 pg $cm^{-2}$ for 5 nm) while variation in Pt:C ratio also impacts measured dissolution. The total amount of Pt loss is 2-3 fold higher for 50 vs. 20 wt.% Pt/C (Figure 1h), ca. 5 nm, 3.9 pg $cm^{-2}$ for 20 wt.% versus 8.9 pg $cm^{-2}$ $s^{-1}$ for 50 wt.%, despite similar electrochemical surface area (ECSA, Figure 1g), and same Pt mass over glassy carbon electrode. These results indicate that 3D porous morphology of the catalyst layer, plays a significant role in assessed dissolution rates, and controlling both particle size and Pt:C ratio influence activity and durability through transport limitations as well as Pt ions release from the 3D layer. Therefore, measuring the true rates of Pt dissolution from nanoparticles would require direct exposure to the electrolyte, without scavenging effect from the porous matrix. This is achieved with sputtered thin films of Pt deposited onto a surface of glassy carbon electrode with known geometric surface area. In order to mimic real nanoparticles, deposition parameters for magnetron sputtering are tuned to attain thin film topology with high angle grain boundaries and homogeneous grain size distribution centered about 3 and 5 nm (confirmed by Scanning Tunneling Microscopy (STM) in Figure S2) [42,43]. Such thin film combines aspects of both extended 2D surfaces and nanoparticles without the influence on eluted metal ion transport and dissolution/redeposition that is imparted by the 3D layer. Namely, an electrode with well-defined geometric surface area and tuned surface morphology resembling that of Pt nanoparticles; however, with lower ECSA due to interconnected-coalesced grains yet with notable roughness factor when compared to flat 2D electrode surfaces.

A comparison between dissolution rates for nanoparticles and those measured on extended 2D single crystalline and thin film surfaces requires normalization of dissolved Pt by ECSA (Figure 1g). This points towards a new metric, spelled as *intrinsic dissolution,* $\Gamma^0$ (ng $cm_{Pt}^{-2}$). Similarly to the $j_k$, intrinsic specific activity for electrochemical reaction rate, this value depicts unique character of each surface depending on geometric arrangement of surface atoms, i.e., coordination number, potential window, sweep rate, electrolyte properties and temperature.

Figure 1 displays a wide variation of Pt dissolution rates observed on well-defined 2D single crystalline surfaces, having (111) orientation as the most stable as no dissolution occurs under given conditions, a direct consequence of delayed PtO formation, which is taking place only above 1.05 V [34]. However, unlike (111) surface, the (100) and (110) orientations have substantially higher number of under-coordinated surface atoms that leads to higher intrinsic dissolution rates (e.g. 111<100<<110). Similar trend in dissolution is found for nanoparticle size effect. As smaller particles have significant surface fraction of corners and edges, these under-coordinated sites correspond to the (110) surfaces [31,32,44]. The consequence is a 30-fold increase in the intrinsic dissolution rate when the size drops from 5 to 3 nm. Additionally, the rate of Pt loss is 500 times higher on 3 nm particles when compared to (110) surfaces as related to the Gibbs-Thompson effect [30–33,36]. This result provides a quantitative insight for the dissolution of Pt nanoparticles, which is the leading cause for catalyst degradation (Figure S4 and S5), and therefore, developing an effective mitigation strategy is one of the biggest challenges in the fuel cell technology.

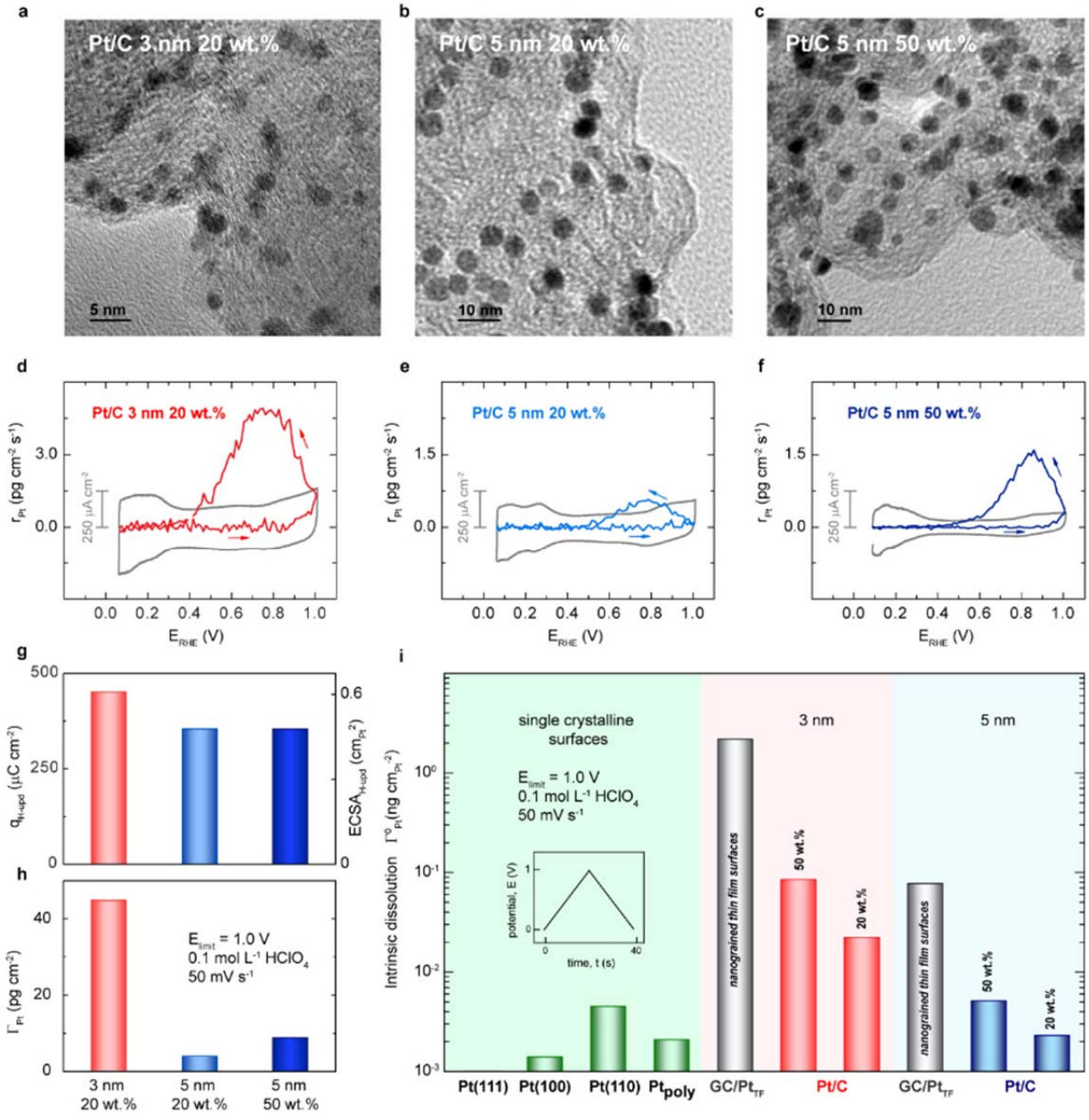


**Figure 1.** – Dissolution trends for Pt surfaces: TEM images of monodispersed Pt nanoparticles of various size and Pt:C ratio **(a)** Pt/C 3 nm 20 wt.%, **(b)** Pt/C 5 nm 20 wt.%, **(c)** Pt/C 5 nm 50 wt.% and corresponding cyclic voltammetry with *in situ* dissolution profiles **(d)**, **(e)** and **(f)** in a single potential cycle between 0.05 and 1.0 V in 0.1 mol $L^{-1}$ $HClO_4$ at 50 mV $s^{-1}$ with 100 rpm at 25°C. **(g)** Uniform Pt loading is confirmed by integrated $H_{upd}$ charge and ECSA retrieved from voltammetry for various Pt/C nanoparticles on glassy carbon electrode. **(h)** Total amount of dissolved Pt obtained by integration of the dissolution curves of a single potential cycle. **(i)** Intrinsic dissolution, $\Gamma^0$ (ng $cm_{Pt}^{-2}$), for single crystalline (111), (100), (110) and polycrystalline Pt surfaces (green bars), nanograined Pt thin film surfaces of 3 nm and 5 nm (gray bars), Pt/C nanoparticles of 3 nm with 20 and 50 wt.% (red bars) and 5 nm with 20 and 50 wt.% (blue bars) reveals increasing dissolution trend by lowering carbon content, with maximum values for nanograined thin film surfaces, confirming scavenging role of carbon matrix within its 3D network.

As mentioned above, the variation in the intrinsic dissolution rates for different Pt to carbon ratio, suggests a highly dynamic process between dissolution and redeposition. This is a

159 distinct property of catalyst supported on high surface area carbon that has not been previously
160 addressed, and should be considered when comparing different support/particle configurations
161 and synthesis methods. Comparison between nanograined thin films and corresponding size 20
162 wt.% Pt/C catalysts reveals that unhindered dissolution rates could be up to 100-fold higher,
163 which accounts for almost 99% of dissolved Pt being contained inside the carbon matrix,
164 providing a direct pathway for agglomeration and particle size growth with consequent decrease
165 in electrochemically active surface area. Yet, the remaining 1% loss amount can be seen as
166 migration of Pt out of the catalyst layer, as confirmed in MEA studies where Pt aggregates were
167 found within the polymer membrane near the cathode[45,46]. It is important to note that both
168 processes of particle growth induced by redeposition and escape of Pt ions from the catalyst
169 layer result in a decrease of ECSA and lower fuel cell performance (Figure S4 and S5). These
170 results highlight the importance of utilization of thin film surfaces with tailored nano-
171 morphology, which enable the assessment of the true intrinsic dissolution of nanoscale materials.
172 Most importantly, tuning of the Pt surface morphology at the nanoscale should be towards the
173 (111) structure in order to minimize the number of undercoordinated surface sites. A feasible
174 mitigation strategy for Pt surface dissolution is introduction of more stable and noble Au into the
175 catalyst structure. One strategy relies on partial coverage of Au over Pt surfaces, which could
176 affect the local Pt electronic structure [47,48]. Despite observing little changes in catalytic activity
177 over thousands of AST cycles[47], the main challenge of this method is possible negative effect on
178 ORR catalytic activity due to excessive blocking of Pt surface sites. Alternatively, utilization of
179 Au in subsurface is shown to improve Pt durability [12,49], but the mechanism for stabilization
180 remains elusive. In order to investigate the effect of Au, both mitigation strategies are evaluated
181 here at the atomic level.

182 First, an underlayer of a nanometer scale thick film of Au was coated over UHV cleaned
183 glassy carbon surface followed by deposition of the same amount of Pt as described above, (ca.
184 0.5 and 2 μg $cm^{-2}$, $Pt_{TF}$ of 3 nm and 5 nm respectively). A direct comparison between film
185 morphologies with and without Au in the subsurface is obtained by STM, and shown in Figure
186 2a-c. While size of individual interconnected grains for the thin films consisting of pure Pt over
187 Au remains the same, their surface spatial arrangement is different and exhibits ordering in grain
188 stacking of Pt over Au, as seen in Figure 2b. Atomic resolution images shown in Figures 2c and
189 S6, reveal closely packed (111) structure of Pt surface atoms.

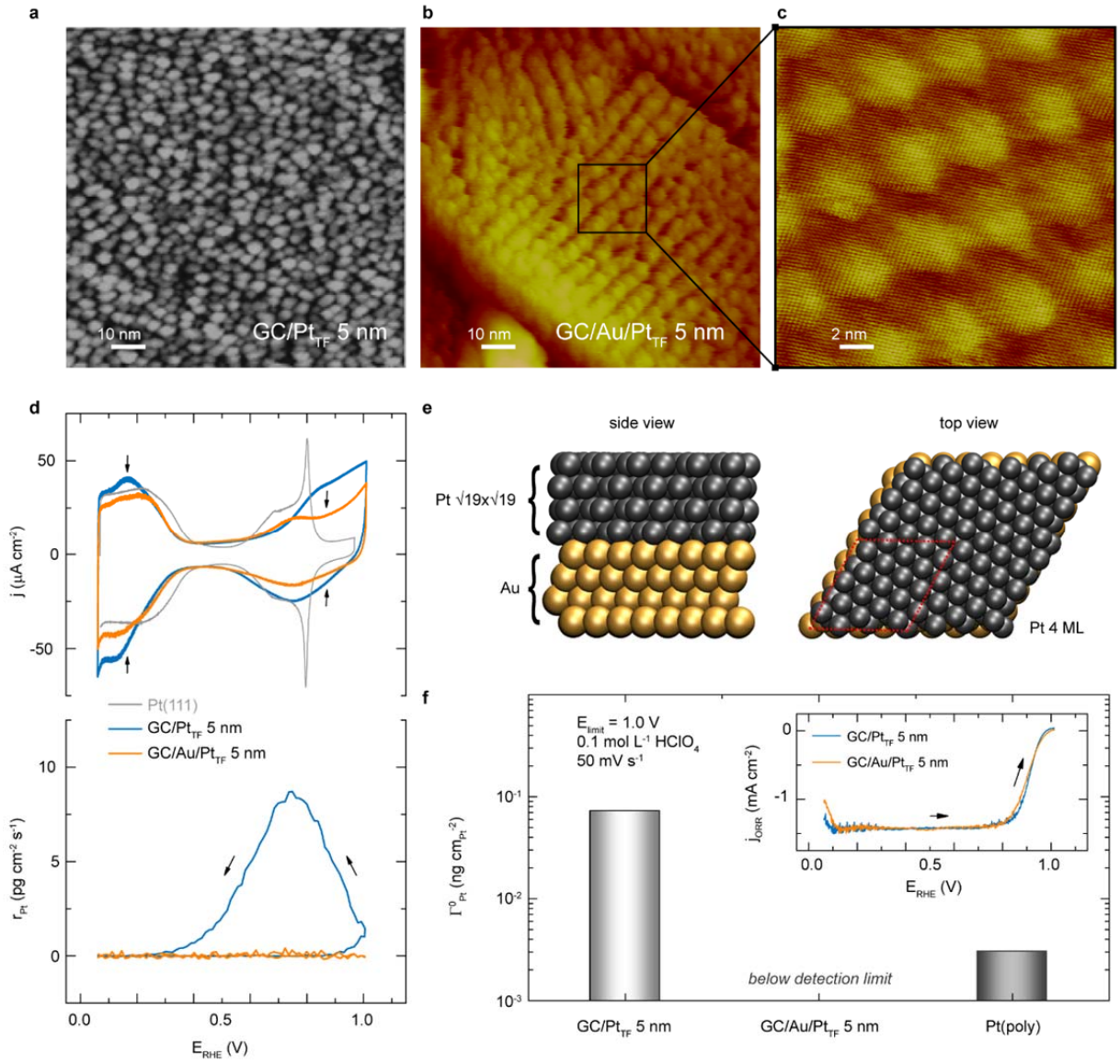


**Figure 2**. The effect of subsurface Au on Pt dissolution rates. STM images (100x100 nm area) of UHV sputtered thin film surfaces with tailored morphology of interconnected Pt grains with uniform 5 nm diameter: **(a)** over bare glassy carbon electrode, **(b)** over thin film of Au deposited on glassy carbon electrode, indicating ordered spatial arrangement in Pt grains stacking, and **(c)** atomic resolution image (20x20 nm area) of **(b)** with ordered and interconnected 5 nm grains, having closely packed (111)-like surface structure of Pt atoms. **(d**, top**)** cyclic voltammogram for GC/Au/Pt$_{TF}$ 5 nm implies surface ordering towards Pt(111) (orange and gray curves), while CV for GC/Pt$_{TF}$ 5 nm (blue curve) resembles polycrystalline Pt features, and **(d**, bottom**)** comparison of dissolution rates obtained by *in situ* RDE-ICP-MS in a single potential cycle. **(e)** Atomistic modelling side and top view representations of most stable Pt layer ($\sqrt{19} \times \sqrt{19}$) formed over a 4x4 Au underlayer. **(f)** Intrinsic dissolution, $\Gamma^0$ (ng $cm_{Pt}^{-2}$), for different Pt thin film surfaces compared to polycrystalline Pt surface. Inset shows ORR polarization curves for both GC/Pt$_{TF}$ 5 nm and GC/Au/Pt$_{TF}$ 5 nm, indicating no change in the ORR kinetics.

Additionally, the CVs in Figure 2d displays pseudo-capacitance indicative of a certain degree of ordering. Specifically, the presence of a featureless current plateau in the $H_{upd}$ region is typical for Pt(111) voltammogram [41], as well as the appearance of a reversible redox feature

between 0.6 and 0.85 V, which is attributed to adsorption/desorption of oxygenated species on Pt(111) surface (so called "butterfly" region). The total charge associated with Pt-OH/O formation is suppressed by the addition of subsurface Au, indicating a decrease in the surface oxophilicity (conversion from polycrystalline to (111)-prevailing surface), while $H_{upd}$ charge remains similar. These findings suggest that the underlayer of Au does promote an atomic scale ordering of the Pt overlayer, resulting in the formation of a Pt(111)-like surface, which in line with Density Functional Theory (DFT) calculations rationalizing overlayer Pt structures (Figure 2e and S7), with important consequences towards Pt dissolution rate.

As observed in Figure 2d (orange curves), the presence of Au underlayer has a profound effect on Pt dissolution rate, eliminating any measurable Pt loss, while no dissolution of Au occurred, (Figure S8). Normalization of the total amount of dissolved Pt by ECSA-$H_{upd}$ (Figure 2f) further confirms the significant improvement of the intrinsic dissolution rate of Pt, making GC/Au/$Pt_{TF}$ 5 nm more stable than Pt(poly), and closely related to Pt(111) (Figure 1i). In addition, the ORR polarization curves for both thin film samples are very similar (inset Figure 2f), indicating that the Au underlayer has minimal effect on the intrinsic ORR activity. This is in-line with our DFT results for the OH binding energy, a typical ORR reactivity descriptor: -2.45 eV on Pt(111) and -2.41 eV on 4 ML of (111)-restructured Pt overlayers, at the low coverage limit (see Table S1 and S2 for details). In the presence of subsurface Au, the enhanced Pt durability extends also to higher potentials, with limited Pt dissolution up to 1.2 V (Figure S9). The confluence of activity and stability is a strong function of the overlayer Pt thickness/loading. Decreasing Pt loading to, ca. 0.5 μg $cm_{geo}^{-2}$ (GC/$Pt_{TF}$ 3 nm) leads to a lower Pt durability with a small loss in ORR activity compared to GC/$Pt_{TF}$ 5 nm (Figure S10). Although the changes to the roughness of the Au substrate film has little impact over Pt stabilization (Figure S9), the high energies involved in the sputter process, in agreement with calculated Pt atom ejection energies (Figure S11b) and the inherent crystal lattice mismatch between Pt and Au that may naturally compress Pt-Pt bonds, could lead to the observed ordering effect (see theoretical modeling in Fig S7). Therefore, optimization of Pt loading, and consequently of particle size leads to a balance between ORR activity and Pt dissolution by promoting surface ordering to (111)-like structure.

Second, the role of surface Au is explored by electrodeposition over Pt(111) surface with sub-monolayer control (ca. 0.04 ML steps, Figure 3a; see method section for details). Atomic

Force Microscopy (AFM) is used to visualize the spatial distribution of Au at different coverage (Figure 3b, d and f), with impact on both ORR and dissolution rates (Figure 3c and e).

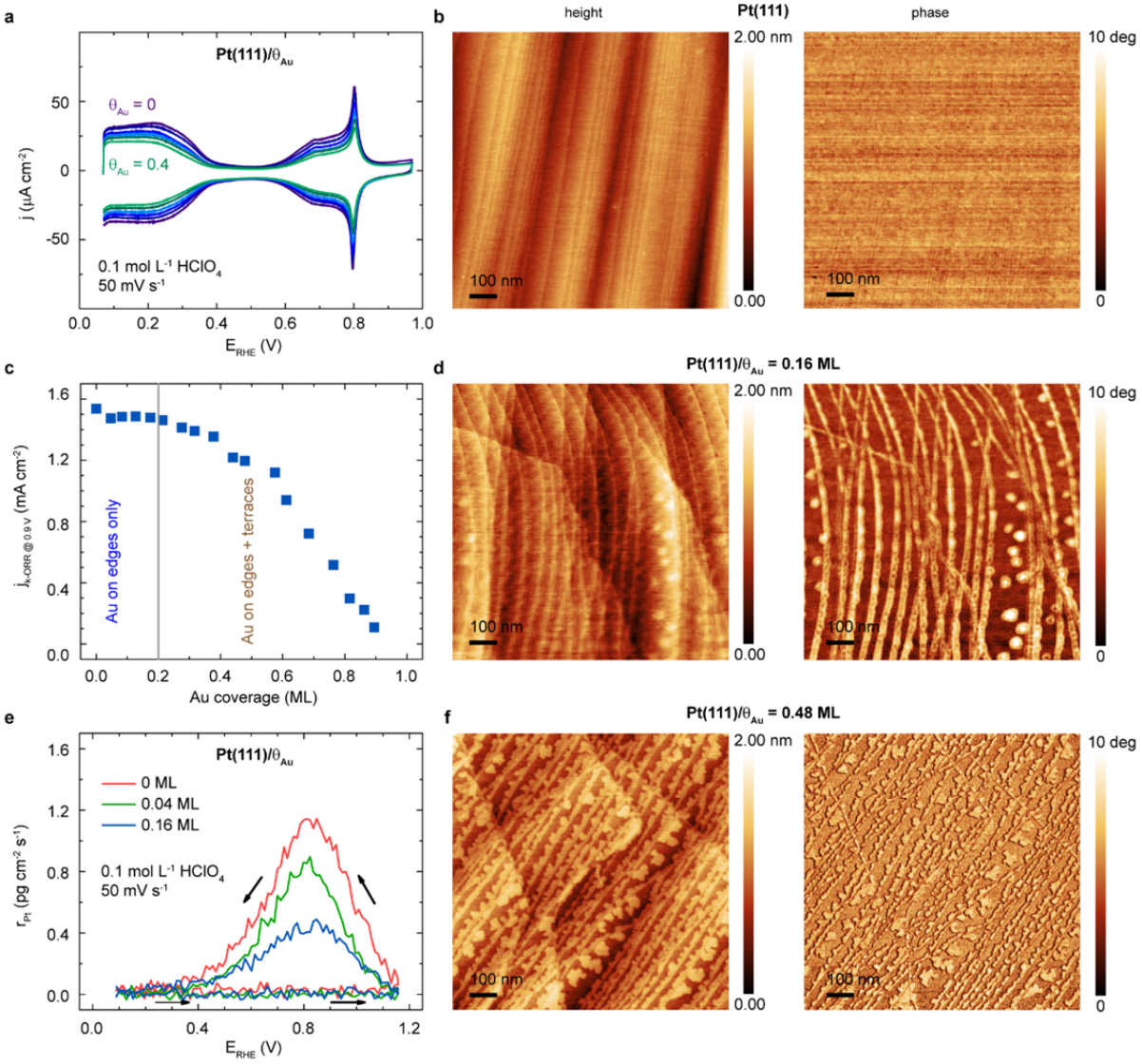


**Figure 3**. Effect of surface Au on Pt(111) dissolution and ORR rates: **(a)** cyclic voltammograms for Pt(111) with different surface coverage of Au. AFM height (left side images) and phase (right side images) contrast 2x2 μm images: **(b)** Pt(111) surface with terraces (50-100 nm wide) and monoatomic step edges, **(d)** Pt(111) with 0.16 ML of Au covering preferentially the step edges sites, **(f)** 0.48 ML of Au spills over to the Pt terraces. **(c)** ORR kinetics for various Au surface coverage ($j_k$ measured at 0.9 V in 0.1 mol $L^{-1}$ $HClO_4$ at 50 mV $s^{-1}$ and 1600 rpm) shows unmodified catalytic activity for $\theta_{Au} < 0.2$ ML. **(e)** Pt dissolution rates for Pt(111) and Au at 0.04 and 0.16 ML measured by SPRDE-ICP-MS by monitoring only the first cycle up to 1.15 V as each subsequent would induce surface roughening.

While Pt(111) surface shows the typical terrace width (50-100 nm, Figure 3b), images for $\theta_{Au} = 0.16$ ML indicate preferential placement of Au atoms at step-edge sites (Figure 3d), followed by spillover onto terraces at higher coverages ($\theta_{Au} = 0.48$ ML, Figure 3f). This selective deposition of Au over undercoordinated sites is confirmed in the voltammetry profile (Figure

3a), as the "wrinkles" from the step-edges in the $H_{upd}$ region are flattened at low Au coverages, while at higher $\theta_{Au}$ both "$OH_{ad}$ butterfly" and $H_{upd}$ features are suppressed, yet preserved. The effect on both ORR rate and surface stability at different stages of Au coverage is assessed (Figures 3c and 3e). At Au coverages up to, ca. $\theta_{Au}$ = 0.2 ML, there is negligible impact on ORR rate, as $j_k$ stays constant at 1.5 mA $cm^{-2}$ at 0.9 V. However, increasing the Au coverage above 0.2 ML results in a measurable decrease in ORR, which coincides with Au spillover on terrace sites. Due to the low intrinsic dissolution of Pt(111) surface, Pt(111)/$\theta_{Au}$ surfaces were cycled up to 1.15 V [34,36,38]. Figure 3e shows the representative Pt dissolution profiles for: $\theta_{Au}$ = 0 ML, $\theta_{Au}$ = 0.04 ML, and $\theta_{Au}$ = 0.16 ML. The selective blockage of undercoordinated step-corner sites has a direct consequence on Pt dissolution rates, as 0.16 ML of Au, (Figure 3b and d), induces a 3-fold decrease in Pt dissolution rate.

Further increase in Au coverage leads only to modest decrease in dissolution rate. Two important findings are obtained, the first is related to Au tendency to neighbor with Pt undercoordinated sites while decreasing their dissolution rates, and the second defines the threshold surface coverage of Au that does not influence the ORR rate but protects Pt from dissolution, emphasizing the optimal coverage of up to 0.2 ML of Au. While more substantial mitigation of Pt dissolution is achieved by (111) texturing through subsurface Au in comparison to surface bound Au, both of these are viable strategies for improving the durability of real-world catalysts. In order to extend these findings towards nanoscale system, a tailored solvothermal synthesis protocol is employed for the targeted compositional profile of PtAu NPs. A one-pot chemical synthesis approach (see methods), derived a series of monodisperse Pt and core-shell PtAu nanoparticle with Pt multilayered shell that should be capable to demonstrate the inherent stabilization imparted by subsurface Au (Figure 4a). For the sake of brevity, only the 3 nm particles are featured here as an ultimate example, since their size makes them the most prone to dissolution (Figures 1 and 2).

Despite the difference in surface energy that would drive gold atoms to occupy surface sites [50], the difference in chemical reduction potential is sufficient to reduce Au at faster rates than Pt atoms during the one-pot synthesis. This balance between the surface energy and kinetics of chemical reaction induces targeted compositional gradient required to keep the majority of Au atoms in the particle core, with only a small portion of Au expected to be on the particle surface.

As mentioned above, Au surface atoms would provide additional passivation of undercoordinated Pt neighboring atoms, maximizing catalyst stability while minimizing impact on the ORR activity.

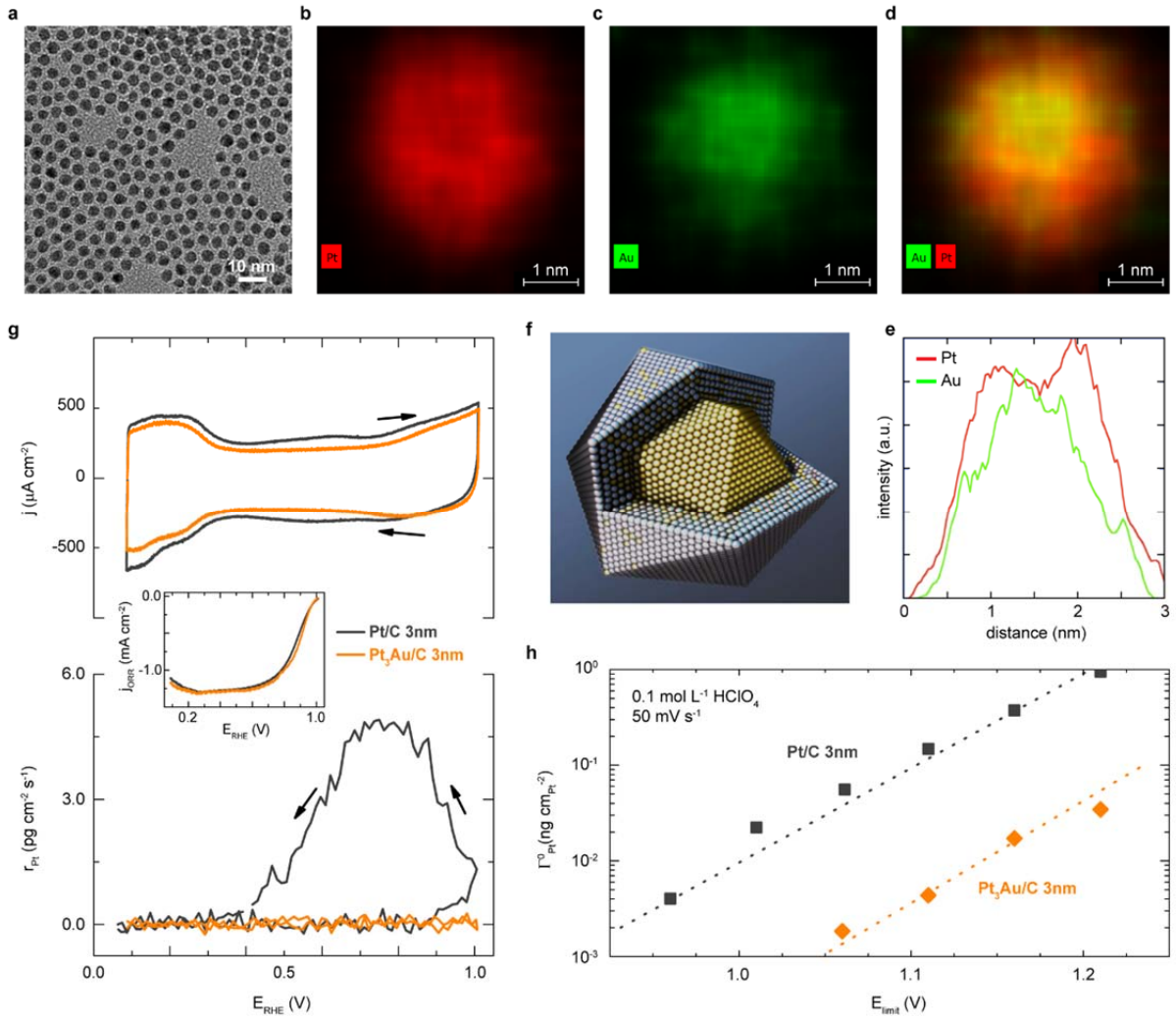


**Figure 4**. – $Pt_3Au$ nanoparticles: **(a)** TEM of as-synthesized particles confirms uniform size distribution of 3 nm. **(b-d)** high-resolution STEM along with elemental mapping acquired by EDS-contrast of Pt, Au and overlayed images, respectively. **(e)** EDS composition line scan in revealing Au-rich core with a Pt shell. **(f)** Illustration of $Pt_3Au$ core-shell nanoparticle with distinct compositional gradient. **(g)** cyclic voltammograms (top curves) and corresponding Pt dissolution profiles (bottom) for Pt/C 3 nm 20 wt.% (gray curves) and $Pt_3Au$/C 3 nm 20 wt.% (orange curve) in 0.1 mol $L^{-1}$ $HClO_4$ at 50 mV $s^{-1}$ and 100 rpm at 25°C. **(h)** Comparison between the intrinsic dissolution of Pt for different positive potential limits (up to 1.2 V) for both pure Pt/C (gray dots) and $Pt_3Au$/C (orange dots) reveals improvement in Pt stability as measured by decrease in dissolution for the wide range of positive potential limits.

The formation of a core-shell nanostructure is confirmed by HR-STEM (Figure 4b, 4c, 4d) where distributions for Au and Pt atoms are obtained by EDS-resolved imaging. The core-shell composition gradient is evident from the EDS line profile for both Au and Pt (Figure 4e), where

the ~ 2 nm diameter Au rich core is surrounded by a ~ 1 nm thick mixed Pt-Au shell, having Pt rich surface (depicted in Figure 4f). The characteristic double peak signature in Pt counts is indicative of a shell structure, while overall composition is confirmed to be $Pt_3Au$. The voltammetry profile shown in Figure 4g is typical for Pt surfaces, noting that both $H_{upd}$ and $OH_{ad}$ regions for $Pt_3Au/C$ system are slightly suppressed compared to Pt/C particles, further supporting the presence of some Au atoms on the surface in the amount of less than 10%.

The combined effect of Au is depicted in the Pt dissolution profile, as cycling the electrode potential up to 1.0 V does not trigger any detectable dissolution from the $Pt_3Au/C$ particles, nor changes to particle size and distribution (Figure S12). Direct comparison to the Pt/C NPs with the same size and loading, reveals staggering difference in dissolution rates, which confirms that the presence of Au eliminates detected Pt dissolution at nanoscale up to 1.0 V even for an extreme example such as 3 nm particles. At the same time, the ORR kinetics (Figure 5g inset) shows similar activity level for both Pt/C and $Pt_3Au/C$ nanoparticles, confirming that the total Au coverage at the surface is below the 20% threshold identified in Figure 3. Further increase in the upper potential limit points to the onset dissolution potential for $Pt_3Au$ particles to be well above 1.0 V however, at substantially lower rates compared to Pt/C NPs (Figure 4h). Direct comparison between the intrinsic dissolution rates for 3 nm particles reveals a consistent over 30-fold improvement for the core-shell particles in the extended potential window beyond 1.2 V. Increasing temperature to 80°C does not change the conclusions regarding Pt dissolution, in fact, it fortifies the effect of Au by eliminating Pt dissolution at potentials relevant for fuel cell operation (Figure S13).

These findings demonstrate that in addition to mere observations of Pt-dissolution, which was considered to be a fundamental limitation of material properties, the intrinsic Pt dissolution of the real-world electrocatalysts can be altered, tuned and even eliminated under given conditions by implementation of the material design rules that have been harvested from high precision evaluations at atomic scale. It is also shown that carbon support is shadowing the real dissolution rates, and for that reason, thin film surfaces with controlled morphology and composition were employed to reveal the true extent of Pt dissolution. Key parameters were controlled to assure that only one variable was changed at the time. That allowed direct atomic scale insight into the well-defined electrochemical interfaces and ability to tune them into robust

highly durable materials. Nevertheless, real electrochemical interface in fuel cells, is more complex, having additional species such as ionomer molecules which are usually randomly and unevenly distributed along and around metal particles, carbon support and carbon matrix pores that can accommodate Pt particles on its surface or inside. That creates substantial uncertainty about consistency of particular interface at the atomic scale, where other factors such as carbon corrosion and ionomer interactions are also taking a toll in overall degradation process. Undoubtedly, these processes should not compromise the intrinsic Pt dissolution rate, as they can only mask it. For those reasons, evaluation of catalyst stability in MEA, which is crucially important, goes beyond the scope of this study. In addition, these results sharply delineate and quantify Pt-dissolution from other degradation routes, which will allow deconvolution of the overall degradation mechanism as well as strategy to mitigate Pt dissolution in more complex structures such as different classes of materials based on Pt-alloys with transition metals that usually come with additional benefits in terms of performance. These findings are foundation for the future work that will address need for the development of an aging algorithm, which will enable accurate durability predictions over thousands hours of operation.

## Methods

**Chemicals:** Hydrogen tetrachloroaurate (III) hydrate ($HAuCl_4.xH_2O$) (99.995%), Chloroplatinic acid hydrate solution ($H_2PtCl_6 \cdot xH_2O$, >99.9%), Oleylamine (OAm, >70%), 1,2,3,4-Tetrahydronaphthalene (99%) and Tetrabutylammonium bromide (TBAB, ≥98.0%) were purchased from Sigma-Aldrich without further purification. Nafion 117 solution (5% in low aliphatic alcohols – water mixture, Sigma-Aldrich) was further diluted in water before mixing with water-based nanoparticle suspension. High purity ultra-trace analysis grade perchloric acid (Omni Trace Ultra, EMD Chemicals) was further purified as described elsewhere [51]. Electrolytes and calibration solutions were prepared with ultra-high purity deionized water (Milli-Q Millipore). Stock solutions of Pt and Au ICP-MS standards (TraceCERT, Sigma-Aldrich) were diluted to the desired concentration with ultra-high purity water and used as calibration standards for ICP-MS. All gases (argon, oxygen, hydrogen) were of 6N quality (Airgas).

**Nanoparticle synthesis (Pt and PtAu):** Synthesis of pure Pt nanoparticles with selected particle size of 3, 5 and 7 nm were performed following the procedures described elsewhere [30,52]. Synthesis of 3 nm $Pt_3Au$ compositional gradient core/shell NPs: In a typical synthesis, under a gentle flow of argon (Ar) and magnetic stirring, 0.25 mmol of hydrogen tetrachloroaurate (III) hydrate ($HAuCl_4.xH_2O$), 6 mL of OAm, and 6 mL of tetralin were mixed at 25°C. The chloroplatinic acid hydrate solution ($H_2PtCl_6 \cdot xH_2O$) in OAm and tetralin (0.75 mmol of $H_2PtCl_6 \cdot xH_2O$ dissolved in 3 mL of OAm and 3 mL of tetralin) was added into the solution.

Then 0.4 mmol TBAB was dissolved in 1 ml of tetralin and 1 ml of OAm via sonication. The solution was then injected into the $HAuCl_4$ solution at 30ºC. The mixture was further heated to 200°C at a heating rate of 4-5°C $min^{-1}$. The solution was kept at this temperature for another 30 min before it was cooled down to room temperature. The product was collected by centrifugation, washed three times with the ethanol/hexane mixture, and then redispersed in hexane.

**Deposition of nano grain Pt thin films:** Thin metal films of Pt and Au were deposited by magnetron sputter deposition[42] on a mirror-polished glassy carbon substrate (base vacuum $1\times10^{-9}$ torr). The deposition rate was calibrated using a quartz-crystal microbalance. For depositing ultra-low loading Pt thin films the deposition rate was set to 0.3 Å $s^{-1}$ while varying the total deposition time and pressure, ~7 s for 0.5 µg $cm^{-2}$ (1ML) and ~30 s for 2 µg $cm^{-2}$ (4ML). Deposition of Au thin film was done at 0.75 Å $s^{-1}$, exposing the glassy carbon surface during approx. 5 min, making a ~20 nm thick film. Ultra low loading of Pt was further deposited over Au thin film by utilizing the same conditions as before. An additional step of thermal annealing was performed on some samples before depositing Pt by heating the sample stage at 400ºC inside the ultra-high vacuum chamber for 1 hour. After cooling the samples to room temperature, Pt deposition proceeded as described before. After deposition is done, the sample is removed from the UHV chamber and embedded into the RDE tip for the electrochemical experiments.

**Deposition of Au submonolayers over Pt single crystal surfaces:** Au overalyers were deposited by electrodeposition method from ultra-diluted Au-containing electrolyte. A solution containing 50-100 ppb of dissolved Au in 0.1 mol $L^{-1}$ $HClO_4$ was used as the deposition electrolyte. Pt single crystal was thermal annealed before deposition as described elsewhere[34]. After surface preparation, Pt(111) was immersed under potential control in the three-electrode deposition cell (0.05 V) and immediately cycled between 0.05 and 0.9 V at 50 mV $s^{-1}$ with electrode rotating at 1600 rpm. After the desired number of deposition cycles, the working electrode was removed, rinsed with ultra-pure deionized and deareated water, and then transferred to another electrochemical cell with clean electrolyte (0.1 mol $L^{-1}$ $HClO_4$). A cyclic voltammetry experiment between 0.05 and 1 V at 50 mV $s^{-1}$ was used to confirm Au coverage by measuring the charge under the $H_{upd}$ desorption region (from 0.05 to 0.4 V).

**High Resolution and Energy Dispersive Spectroscopy mapping:** Scanning transmission electron microscopy (STEM) images were acquired in bright field (BF)-STEM and high angle annular dark field (HAADF)-STEM modes using a JEOL JEM-2200FS aberration-corrected STEM operated at 200 kV. The STEM is equipped with a Bruker X-flash energy dispersive X-ray spectrometer (EDS) for acquisition of Pt and Au elemental maps (spectrum imaging).

**Scanning Tunneling Microscopy:** Characterization of the deposited nano grain thin films of Pt over GC and GC/Au was performed at room temperature in air scanning tunneling microscopy (STM) using a NanoScope III D (Veeco, USA) instrument. We used height imaging mode with a Pt-Ir tip (current set-point around 1-2 nA and bias voltage between 20 to 100 mV). The mean

grain size values were acquired from a few randomly chosen (100x100 nm) areas of STM images.

**Atomic Force Microscopy:** Atomic Force Microscopy imaging in standard tapping mode (Brucker dimension ICON, MA) was used to capture both topography and phase images of the Pt/Au surface simultaneously. All images were made with a Tespa V2 (Brucker, MA) silicon probe with < 7 nm radius. Topography image shows varying in heights across the scan area. Phase imaging is particularly useful in chemical mapping of surface as it is sensitive to surface stiffness/softness and adhesion between the tip and surface. The AFM data were processed and analyzed using the Gwyddion software package. Image backgrounds are removed using line by line correction.

**Preparation of Catalyst Layer for Electrochemistry:** The as-synthesized NPs were first deposited onto carbon support (Tanaka 902.4 $m^2\ g^{-1}$) in hexane under sonication to make NP/C catalyst. The catalyst was further annealed at 185°C to remove residual surfactant (capping agent) before they were collected via centrifugation (8500 rpm, 8 min) and washed with ethanol twice. The 3 nm $Pt_3Au$/C catalysts were dispersed in Milli-Q water under sonication to make around 0.5 mg $mL^{-1}$ catalyst ink. The catalyst inks were prepared to be 0.01% Nafion solution by adding the appropriate amount of 5% Nafion 117 solution (The Pt/C ratio for the $Pt_3Au$ catalysts is 18.9 wt.% measured by ICP-MS). The made ink was pipetted onto the glassy carbon (GC) electrode surface (0.283 $cm^2$ geometrical surface area) to make the working electrode with Pt loadings of ca. 6 $\mu g_{Pt}\ cm^{-2}$. Other Pt NPs catalysts electrode were made by the similar method and desired Pt loading on the GC surface. The nanoparticle results are shown after "pre-cycling" the electrodes from 0.05 V up to 0.95 V at 50 $mVs^{-1}$ for 50 cycles.

**Electrochemical experiments:** All the electrochemical experiments were done with an Autolab PGSTAT 302N potentiostat (Metrohm), a standard three-electrode electrochemical cell purged with either argon or $O_2$, and a rotating disk electrode (RDE) setup. All working electrodes were 6 mm outer diameter disks (GC and Pt single crystals) reversibly embedded on a Teflon cup and further secured in a PCTFE collet that engages with the rotating shaft of the RDE rotor. A carbon rod (99.99995%, Alfa-Aesar) and a bridged Ag/AgCl reference electrode (BASi) were employed as counter and reference electrode, respectively, for all electrochemical experiments. Separate carbon counter electrodes were used for electro-deposition experiment. All electrode potential are shown versus the reversible hydrogen electrode (RHE), calibrated from a separate experiment using $H_2$ oxidation and reduction cycles. Typical cyclic voltammetry (CV) experiments were performed by cycling from 0.05 up to 1 V at 50 mV $s^{-1}$. Additional experiments varying the upper potential limit from 1 V up to 1.2 V were also executed to evaluate the amounts of dissolution at elevated electrode potentials. All experiments were done by rotating the electrode at 100 rpm, unless otherwise indicated. All experiments were obtained with solution iR compensation. All the tests were conducted at ambient pressure at room temperature and 80$^oC$.

***In Situ* ICP-MS experiments:** Simultaneous electrochemical and Pt dissolution rates measurements were done by attaching a stationary probe to the RDE (SPRDE method [34]), and the fraction of electrolyte pumped from the electrode surface was analyzed directly into an ICP-MS (Perkin Elmer, NexION 350S). Plasma, auxiliary and nebulization flow rates were 15.6 L $min^{-1}$, 1 L $min^{-1}$ and 1 L $min^{-1}$, respectively, and plasma RF power set to 1600 W. Pt (195 a.m.u) and Au (197 a.m.u) ions were simultaneously measured in the ICP-MS at a 4 points per second total, while the working electrode was controlled by the potentiostat as described above. The SPRDE collection efficiency at these conditions is 0.25[34].

**Theoretical Methods:** Periodic density functional theory (DFT) calculations were performed using the Vienna Ab Initio Simulation Package (VASP) [53,54]. Projector augmented wave (PAW) potentials were used to describe the core electron interactions. A plane wave basis set with a kinetic energy cutoff of 400 eV was used to expand the electronic wave function of the valence electrons. The generalized gradient approximation (GGA) using the Perdew, Burke, and Ernzerhof (PBE) exchange-correlation functional was used [55]. Geometry optimizations were performed until the Hellman−Feynman forces on each atom were less than 0.01 eV $Å^{-1}$. With these settings, the Pt and Au optimized bulk lattice constants were determined to be 3.970 Å and 4.158 Å, in good agreement with the experimental values of 3.92 Å and 4.14 Å[56], respectively.

Unless otherwise stated (see **Error! Reference source not found.**), 4×4 periodic supercells, comprising 4 Au underlayers and from 1 to 4 Pt overlayers, were used. The bottom two layers of the slab were kept fixed at the bulk lattice positions while all the remaining layers were fully relaxed. We included at least 15 Å of vacuum between successive slabs (in the z-direction), to avoid spurious interactions between periodic replicas. For these supercells, the first Brillouin zone was sampled with a (4×4×1) Monkhorst–Pack *k*–point mesh [57].

To rationalize stability against dissolution and ORR activity trends, as well as the texturing effect on Pt, induced by the Au underlayers, we constructed several surface Pt/Au slab models. Among these, we evaluated the stability of three classes of surface models: 1) "stoichiometric" Pt overlayers on Au, where the ratio between Pt and Au atoms in the adjacent two layers of the slab defining the Pt/Au interface is 1; 2) "Non-stoichiometric" Pt overlayers on Au, in which the ratio between Pt and Au atoms at the Pt/Au interface is greater than 1; 3) single atom alloys-like surface models, in which a single Au atom substitutes for a Pt atom in the topmost (stoichiometric) Pt layer of the slab. The stability of these surface models was evaluated using two different descriptors, namely the surface energy and the "Pt ejection energy".

The surface energy (Γ) was defined as:

$$\Gamma = (E_{Tot} - N_{Pt}E_{Pt\ bulk} - N_{Au}E_{Au\ bulk})/2A$$

Where $E_{Tot}$ is the total electronic energy of the slab, $N_{Pt}$ is the number of Pt atoms in the slab, $N_{Au}$ is the total number of Au atoms in the slab, $E_{Pt\ bulk}$ is the energy of a Pt atom in bulk Pt, $E_{Au\ bulk}$ is the energy of an Au atom in bulk Au, and A is the surface area of the unit cell.

The Pt ejection energy ($E_{eject}$) was calculated using the following expression:

$$E_{eject} = (E_{Pt} + E_{Tot\text{-}Pt}) - E_{Tot}$$

where $E_{Pt}$ is the gas-phase energy of a Pt atom, $E_{Tot}$ is the total energy of the intact slab, comprising Pt and Au atoms, and $E_{Tot\text{-}Pt}$ is the energy of the slab in which a Pt atom has been removed from its topmost layer. $E_{eject}$ is a descriptor of the stability of the Pt overlayer, which can be compared with the experimentally observed Pt dissolution trends. The more positive the $E_{eject}$, the more stable Pt is against dissolution.

All the energy terms used for the calculation of $\Gamma$ and $E_{eject}$ are obtained after geometry optimization of respective initial and final states.

Binding energy of OH (BE) on the studied surface models were obtained using the following expression:

$$BE = E_{Surf+OH} - (E_{Surf} + E_{OH})$$

where $E_{Surf+OH}$ is the total electronic energy of the most stable OH adsorption configuration on the respective slab, $E_{Surf}$ is the electronic energy of the clean slab, and $E_{OH}$ is the gas-phase energy of OH. Spin-polarization had a negligible effect on the calculated total energy. All systems had ground state with zero net magnetic moment.

## Data Availability Statement

All data are available in the main text and in the supplementary information, and available from corresponding author upon reasonable request. Data for bar graphs are available in the Source Data files.

## References


1. Turner, J. A. Sustainable Hydrogen Production. *Science* **305**, 972–974 (2004).

2. Stamenkovic, V. R., Strmcnik, D., Lopes, P. P. & Markovic, N. M. Energy and fuels from electrochemical interfaces. *Nat. Mater.* **16**, 57–69 (2016).

3. Eberle, U. & Von Helmolt, R. Sustainable transportation based on electric vehicle concepts: A brief overview. *Energy Environ. Sci.* **3**, 689–699 (2010).

4. Yoshida, T. & Kojima, K. Toyota MIRAI fuel cell vehicle and progress toward a future hydrogen society. *Electrochem. Soc. Interface* **24**, 45–49 (2015).

5. Gittleman, C. S., Kongkanand, A., Masten, D. & Gu, W. Materials research and development focus areas for low cost automotive proton-exchange membrane fuel cells. *Curr. Opin. Electrochem.* **18**, 81–89 (2019).

6. Bu, L. *et al.* Biaxially strained PtPb/Pt core/shell nanoplate boosts oxygen reduction catalysis. *Science* **354**, 1410–1414 (2016).

7. Li, M. *et al.* Ultrafine jagged platinum nanowires enable ultrahigh mass activity for the oxygen reduction reaction. *Science* **354**, 1414–1419 (2016).

8. Stephens, I. E. L., Rossmeisl, J. & Chorkendorff, I. Toward sustainable fuel cells. *Science* **354**, 1378–1379 (2016).

9. Wang, L. *et al.* Tunable intrinsic strain in two-dimensional transition metal electrocatalysts. *Science* **363**, 870–874 (2019).

10. Chattot, R. *et al.* Surface distortion as a unifying concept and descriptor in oxygen reduction reaction electrocatalysis. *Nat. Mater.* **17**, 827–833 (2018).

11. Escudero-Escribano, M. *et al.* Tuning the activity of Pt alloy electrocatalysts by means of the lanthanide contraction. *Science* **352**, 73–76 (2016).

12. Kang, Y. *et al.* Multimetallic core/interlayer/shell nanostructures as advanced electrocatalysts. *Nano Lett.* **14**, 6361–6367 (2014).

13. Strasser, P. *et al.* Lattice-strain control of the activity in dealloyed core-shell fuel cell catalysts. *Nat. Chem.* **2**, 454–460 (2010).

14. Ye, X., Ruban, A. V. & Mavrikakis, Manos. Adsorption and dissociation of O2 on Pt-Co and Pt-Fe Alloys. *J. Am. Chem. Soc.* **126**, 4717–4725 (2004).

15. Chen Chen *et al.* Highly Crystalline Multimetallic Nanoframes with Three-Dimensional Electrocatalytic Surfaces. *Science* **343**, 1339–1343 (2014).

16. Stamenkovic, V. R. *et al.* Improved oxygen reduction activity on Pt3Ni(111) via increased surface site availability. *Science* **315**, 493–7 (2007).

17. Ferreira, P. J. *et al.* Instability of Pt/C electrocatalysts in proton exchange membrane fuel cells: A mechanistic investigation. *J. Electrochem. Soc.* **152**, 2256–2271 (2005).

18. Shao-Horn, Y. *et al.* Instability of supported platinum nanoparticles in low-temperature fuel cells. *Top. Catal.* **46**, 285–305 (2007).

19. Borup, R. *et al.* Scientific aspects of polymer electrolyte fuel cell durability and degradation. *Chem. Rev.* **107**, 3904–3951 (2007).

20. Mayrhofer, K. J. J. *et al.* Non-destructive transmission electron microscopy study of catalyst degradation under electrochemical treatment. *J. Power Sources* **185**, 734–739 (2008).

21. Mayrhofer, K. J. J. *et al.* Fuel cell catalyst degradation on the nanoscale. *Electrochem. commun.* **10**, 1144–1147 (2008).

22. Takahashi, I. & Kocha, S. S. Examination of the activity and durability of PEMFC catalysts in liquid electrolytes. *J. Power Sources* **195**, 6312–6322 (2010).

23. Wang, X., Kumar, R. & Myers, D. J. Effect of voltage on platinum dissolution relevance to polymer electrolyte fuel cells. *Electrochem. Solid-State Lett.* **9**, 225–227 (2006).

24. Pizzutilo, E. *et al.* On the need of improved Accelerated Degradation Protocols (ADPs): Examination of platinum dissolution and carbon corrosion in half-cell tests. *J. Electrochem. Soc.* **163**, F1510–F1514 (2016).

25. Meier, J. C. *et al.* Degradation mechanisms of Pt/C fuel cell catalysts under simulated start-stop conditions. *ACS Catal.* **2**, 832–843 (2012).

26. Hodnik, N. *et al.* Severe accelerated degradation of PEMFC platinum catalyst: A thin film IL-SEM study. *Electrochem. commun.* **30**, 75–78 (2013).

27. Uchimura, M. & Kocha, S. The impact of cycle profile on PEMFC durability. *ECS Trans.* **11**, 1215–1226 (2007).

28. Wilson, M. S., Garzon, F. H., Gottesfeld, S. & Kurt, E. Surface Area Loss of Supported Platinum in Polymer Electrolyte Fuel Cells. *J. Electrochem. Soc.* **140**, 2872–2877 (1993).

29. Smith, M. C., Gilbert, J. A., Mawdsley, J. R., Seifert, S. & Myers, D. J. In situ small-angle X-ray scattering observation of Pt catalyst particle growth during potential cycling. *J. Am. Chem. Soc.* **130**, 8112–8113 (2008).

30. Li, D. *et al.* Functional links between Pt single crystal morphology and nanoparticles with different size and shape: The oxygen reduction reaction case. *Energy Environ. Sci.* **7**, 4061–4069 (2014).

31. Tang, L. *et al.* Electrochemical stability of nanometer-scale Pt particles in acidic environments. *J. Am. Chem. Soc.* **132**, 596–600 (2010).

32. Tang, L., Li, X., Cammarata, R. C., Friesen, C. & Sieradzki, K. Electrochemical stability of elemental metal nanoparticles. *J. Am. Chem. Soc.* **132**, 11722–11726 (2010).

33. Topalov, A. A. *et al.* Dissolution of Platinum: Limits for the Deployment of Electrochemical Energy Conversion? *Angew. Chemie Int. Ed.* **51**, 12613–12615 (2012).

34. Lopes, P. P. *et al.* Relationships between Atomic Level Surface Structure and Stability/Activity of Platinum Surface Atoms in Aqueous Environments. *ACS Catal.* **6**, 2536–2544 (2016).

35. Cherevko, S. *et al.* Dissolution of Platinum in the Operational Range of Fuel Cells. *ChemElectroChem* **2**, 1471–1478 (2015).

36. Lopes, P. P. *et al.* Dynamics of electrochemical Pt dissolution at atomic and molecular levels. *J. Electroanal. Chem.* **819**, 123–129 (2018).

37. Pavlišič, A. *et al.* Platinum dissolution and redeposition from Pt/C fuel cell electrocatalyst at potential cycling. *J. Electrochem. Soc.* **165**, F3161–F3165 (2018).

38. Jacobse, L., Huang, Y. F., Koper, M. T. M. & Rost, M. J. Correlation of surface site

formation to nanoisland growth in the electrochemical roughening of Pt(111). *Nat. Mater.* **17**, 277–282 (2018).

39. Ott, S. *et al.* Ionomer distribution control in porous carbon-supported catalyst layers for high-power and low Pt-loaded proton exchange membrane fuel cells. *Nat. Mater.* **19**, 77–85 (2020).

40. Sui, S. *et al.* A comprehensive review of Pt electrocatalysts for the oxygen reduction reaction: Nanostructure, activity, mechanism and carbon support in PEM fuel cells. *J. Mater. Chem. A* **5**, 1808–1825 (2017).

41. Markovic, N. M. & Ross Jr., P. N. Surface science studies of model fuel cell electrocatalysts. *Surf. Sci. Rep.* **45**, 117–229 (2002).

42. Van Der Vliet, D. F. *et al.* Mesostructured thin films as electrocatalysts with tunable composition and surface morphology. *Nat. Mater.* **11**, 1051–1058 (2012).

43. Snyder, J. *et al.* Thin Film Approach to Single Crystalline Electrochemistry. *J. Phys. Chem. C* **117**, 23790–23796 (2013).

44. Kinoshita, K. *Electrochemical Oxygen Technology*. (John Wiley & Sons, 1992).

45. Bi, W., Gray, G. E. & Fuller, T. F. PEM fuel cell PtC dissolution and deposition in nafion electrolyte. *Electrochem. Solid-State Lett.* **10**, 101–104 (2007).

46. Macauley, N. *et al.* Pt Band formation enhances the stability of fuel cell membranes. *ECS Electrochem. Lett.* **2**, 33–35 (2013).

47. Zhang, J., Sasaki, K., Sutter, E. & Adzic, R. R. Stabilization of Platinum Oxygen-Reduction Electrocatalysts Using Gold Clusters. *Science* **315**, 220–222 (2007).

48. Kodama, K., Jinnouchi, R., Takahashi, N., Murata, H. & Morimoto, Y. Activities and Stabilities of Au-Modified Stepped-Pt Single-Crystal Electrodes as Model Cathode Catalysts in Polymer Electrolyte Fuel Cells. *J. Am. Chem. Soc.* **138**, 4194–4200 (2016).

49. Wang, C. *et al.* Multimetallic Au/FePt3 nanoparticles as highly durable electrocatalyst. *Nano Lett.* **11**, 919–926 (2011).

50. Ruban, A. V., Skriver, H. L. & Nørskov, J. K. Surface segregation energies in transition-metal alloys. *Phys. Rev. B - Condens. Matter Mater. Phys.* **59**, 15990–16000 (1999).

51. Strmcnik, D. *et al.* When Small is Big: The Role of Impurities in Electrocatalysis. *Top. Catal.* **58**, 1174–1180 (2015).

52. Li, D. *et al.* Surfactant removal for colloidal nanoparticles from solution synthesis: The effect on catalytic performance. *ACS Catal.* **2**, 1358–1362 (2012).

53. Kresse, G. & Furthmüller, J. Efficiency of ab-initio total energy calculations for metals and semiconductors using a plane-wave basis set. *Comput. Mater. Sci.* **6**, 15–50 (1996).

54. Kresse, G. & Furthmüller, J. Efficient iterative schemes for ab initio total-energy calculations using a plane-wave basis set. *Phys. Rev. B - Condens. Matter Mater. Phys.* **54**, 11169–11186 (1996).

55. Perdew, J. P., Burke, K. & Ernzerhof, M. Generalized gradient approximation made simple. *Phys. Rev. Lett.* **77**, 3865–3868 (1996).

56. Haynes, W. M., Bruno, T. J., Lide, D. R., E. . Properties of the Elements and Inorganic Compounds. *CRC Handbook of Chemistry and Physics, 95th ed.* 145–152 (2015).

57. Monkhorst, H. J. & Pack, J. D. Special points for Brillouin-zone integrations. *Phys. Rev. B* **13**, 5188–5192 (1976).

## Acknowledgements

This work was done at Argonne National Laboratory which is operated for the DOE Office of Science by UChicago Argonne, LLC, under contract number DE-AC02-06CH11357. The research efforts on single crystalline systems, well-defined thin films and in-situ dissolution measurements were supported by the Office of Science, Office of Basic Energy Sciences, Materials Sciences and Engineering Division. Synthesis and characterization of nanoscale materials was supported by the U.S. Department of Energy, Office of Energy Efficiency and Renewable Energy, Vehicle Technologies Office. Transmission electron microscopy studies

were accomplished at the Center for Nanoscale Materials, at Argonne National Laboratory, an Office of Science user facility supported by the U.S. Department of Energy, Office of Science, Office of Basic Energy Sciences, under Contract No. DE-AC02- 06CH11357, and at Center for Nanophase Materials Sciences at Oak Ridge National Laboratory, an Office of Science user facility supported by the U.S. Department of Energy, Office of Science, Office of Basic Energy Sciences, with work supported by the Hydrogen & Fuel Cell Technologies Office, Energy Efficiency and Renewable Energy, U.S. Department of Energy. Computational modeling work at UW-Madison was supported by the Department of Energy-Basic Energy Sciences, Division of Chemical Sciences (Grant DE-FG02-05ER15731); and was partially performed using supercomputer resources at National Energy Research Scientific Computing Center (NERSC). NERSC is supported by the U.S. DOE, Office of Science under Contract No. DE-AC02-05CH11231.

## Author Contributions

P.P.L., H.D., C.W and V.R.S. conceived the idea and designed the experiments. P.P.L. performed in situ dissolution measurements on all systems. C.W., D.L. and J.S. developed and performed thin film depositions. H.L., Y.K., N.B. and D.L. performed synthesis and characterization of nanoscale materials. M.M. and R.S. designed and performed the theoretical modeling work. D.T. and Y.S. performed scanning tunneling and atomic-force microscopy measurements. K.L.M. performed high-resolution STEM and EDS characterizations. P.P.L., D.L., D.S., M.M., N.M.M. and V.R.S. analyzed and discussed the results. C.W., P.P.L., and V.R.S. drafted the manuscript. V.R.S. supervised the research. All authors approved the final version of the manuscript.

## Competing interests

The authors declare no competing financial interest.

## Additional Information

**Supplementary information** is available for this paper at (manuscript website link)

**Correspondence and requests for materials** should be addressed to V.R.S.

**Reprints and permissions information** is available at www.nature.com/reprints